UDK 661.871:542.973
Original scientific article/Izvirni znanstveni članek

ISSN 1580-2949
Mater. Tehnol.

PREPARATION OF NANO MANGANESE OXIDE AND ITS APPLICATION IN THE WET OXIDATION OF PHENOL

PRIPRAVA NANO MANGANOVEGA OKSIDA IN NJEGOVA UPORABA PRI MOKRI OKSIDACIJI FENOLA

Weitao Huo, Hongjing Yuan*, Yongchao Hao, Cuige Lu, Lixia Wang, Mengdi Cao

College of Chemical Engineering and Biotechnology, Xingtai University, Xingtai 054000

Prejem rokopisa – received: 2025-12-05; sprejem za objavo – accepted for publication: 2026-04-10

doi:10.17222/mit.2025.1625

Manganese oxide nanoparticles have application prospects in catalysis due to their high specific surface area, abundant active sites, and excellent chemical stability. In this study, nano α-Mn_2O_3 catalysts were synthesized via microwave-assisted carbonization in a glucose-urea system. Characterization results revealed that the amount of urea added influences the structure of the prepared manganese oxide, the optimized sample, Mn-3 possessed the smallest crystallite size, the highest specific surface area, and a mesoporous structure. In the catalytic wet oxidation of phenol, Mn-3 demonstrated a remarkable conversion rate of 97.8 %, significantly outperforming α-Mn_2O_3 prepared by conventional precipitation methods of 58.8 %. Recycling tests indicated that Mn-3 retained a 60 % conversion efficiency after five cycles, demonstrating good stability. This superior performance was attributed to its abundant surface defects, high specific surface area, and mesoporous structure.

Keywords: Nano manganese oxide; Deep eutectic solvent; Phenol; Catalytic wet air oxidation

Nanodelci manganovega oksida imajo velike možnosti za uporabo v katalizi zaradi svoje visoke specifične površine, številnih aktivnih mest in odlične kemijske stabilnosti. V tem članku avtorji opisujejo študijo sinteze nano katalizatorja α-Mn_2O_3 z mikrovalovno podprto karbonizacijo v sistemu glukoza-sečnina. Rezultati karakterizacije so pokazali, da količina dodane sečnine pomembno vpliva na strukturo pripravljenega manganovega oksida, optimiziran vzorec Mn-3 pa je imel najmanjšo velikost kristalitov, največjo specifično površino in mezoporozno strukturo. Pri katalitični mokri oksidaciji fenola je Mn-3 pokazal izjemno stopnjo pretvorbe 97,8 %, kar znatno presega α-Mn_2O_3, pripravljen s konvencionalnimi metodami obarjanja, ki znaša 58,8 %. Preskusi recikliranja so pokazali, da je Mn-3 po petih ciklih ohranil 60-odstotno učinkovitost pretvorbe, kar kaže na dobro stabilnost. To vrhunsko učinkovitost so avtorji raziskave pripisali njegovim številnim površinskim napakam, visoki specifični površini in mezoporozni strukturi.

Ključne besede: nano manganov oksid, globoko evtektično topilo, fenol, katalitična oksidacija z mokrim zrakom

1 INTRODUCTION

Industrial wastewater generated from manufacturing, agriculture, and domestic activities frequently contains high concentrations of phenolic compounds. Without effective treatment prior to discharge, such wastewater poses severe risks to aquatic ecosystems and human health. Conventional treatment methods – such as biodegradation, adsorption, and chemical oxidation – often suffer from limited efficiency, high operational costs, or the generation of secondary pollutants when applied to high-strength, toxic phenolic streams.[1] In response, the development of efficient and environmentally sustainable Advanced Oxidation Processes (AOPs) has emerged as a key research priority. Among these, Catalytic Wet Air Oxidation (CWAO) has attracted considerable interest due to its unique capability to degrade refractory organic pollutants under mild conditions.[1,2] The efficacy of CWAO is largely governed by the catalyst's performance. Transition-metal oxides, in particular, have been extensively studied owing to their excellent redox properties and structural tunability.

Among transition-metal oxides, manganese oxides have garnered attention due to their low cost, environmental compatibility, and exceptional redox properties.[3] Their catalytic activity in CWAO is fundamentally rooted in a Mars-van-Krevelen-type mechanism, where lattice oxygen participates in the oxidation of organic substrates, creating surface-oxygen vacancies.[4] These vacancies subsequently activate molecular oxygen from the solution, replenishing the lattice oxygen and completing the catalytic cycle. The superior performance of MnO_x is attributed to the flexible coexistence of multiple oxidation states (Mn^{2+}, Mn^{3+}, Mn^{4+}), which facilitates this redox cycling.[5] Furthermore, the abundance of surface oxygen vacancies on nanostructured MnO_x serves as the primary active sites for O_2 activation and subsequent radical generation. Consequently, the catalytic performance is intrinsically linked to the material's structural properties, including crystal phase, morphology, specific surface area, and defect density. For instance, Yang et al. demonstrated that γ-MnO_2 and amorphous MnO_2 achieved high phenol-removal efficiencies, attributing this to the formation of surface Mn(III)–$(HO)OSO_3$ com-

*Corresponding author's e-mail:
xtxychem@126.com (Hongjing Yuan)

plexes that enable a nonradical electron-transfer pathway.[6] Similarly, Zhang et al. reported that mesoporous γ-MnO_2, synthesized via a hard-templating method, exhibited enhanced performance in catalytic ozonation, underscoring the critical role of mesoporosity in facilitating mass transfer and providing abundant active sites.[7] These studies collectively highlight that the rational design of MnO_x catalysts with tailored structural features is key to unlocking their full potential in CWAO.

Despite these advances, the controllable synthesis of MnO_x with optimized structural and surface properties remains a critical focus in the field. To address this, various methods – such as co-precipitation, sol-gel processing, and hydrothermal synthesis – have been extensively developed and employed to achieve precise control over the particle size, morphology, and defect chemistry of manganese oxides. Concurrently, considerable research has been dedicated to improving the simplicity of synthetic procedures, reducing solvent consumption, minimizing the use of toxic reagents, and enhancing the activity and stability of the resulting catalysts.[8] These endeavors have advanced the understanding and application of MnO_x in catalytic systems.

In response to this challenge, our research group recently developed a novel synthetic platform utilizing a glucose-urea deep-eutectic system. This method leverages the unique properties of the deep-eutectic solvent, which acts as both a reaction medium and a structure-directing agent[9]. During microwave-assisted carbonization, urea serves as a porogen and nitrogen source, while glucose provides a carbonaceous matrix, facilitating the formation of small, well-dispersed metal oxide nanoparticles with high specific surface areas and abundant mesoporosity. Compared to traditional synthesis methods, this glucose-urea approach offers several distinct advantages: (1) it is a one-pot, solvent-free process that aligns with green-chemistry principles; (2) the urea content can be easily tuned to precisely control the crystallite size, surface area, and defect structure of the resulting oxides; and (3) the mild synthesis conditions and short reaction times are energy-efficient. This strategy has been successfully employed in our previous work for the synthesis of high-performance ceria nanomaterials.

Building upon this foundation, the present study aims to extend this novel glucose-urea-mediated synthesis to nanostructured manganese oxides and evaluate their catalytic performance in the CWAO of phenolic wastewater, using phenol as a model pollutant. By systematically investigating the influence of synthesis parameters on the structural and catalytic properties of MnO_x, this work seeks to establish a structure–activity relationship and develop an efficient, stable catalyst for the green treatment of phenolic wastewater.

2 EXPERIMENTAL PART

2.1 Material Preparation

The basic synthesis procedure was as follows: 3 g of glucose and a certain amount of urea were weighed and thoroughly mixed in a beaker. The beaker was then transferred to an oil bath and heated with stirring at 110 °C. Once the mixture melted into a clear and transparent liquid, 2 g of manganese nitrate was added, and stirring continued for 30 min. The beaker was then transferred to a microwave oven and carbonized at 1800 W for 5 min, yielding a black, fluffy solid. After thorough grinding, the precursor was placed in a muffle furnace and calcined at 500 °C for 4 h with a heating rate of 5 °C/min to obtain the final product, nano-manganese oxide. The schematic diagram of the synthesis process is shown in **Figure 1**.

To investigate the effect of urea dosage on the synthesized material, the amount of urea added was varied to 2.5 g, 5 g, 10 g, 15 g, and 20 g. The corresponding samples were labeled as Mn-1, Mn-2, Mn-3, Mn-4, and Mn-5, respectively.

For comparison of the impact of synthesis methods on the product's performance, manganese oxide was also prepared via a precipitation method. The specific procedure was as follows: a certain amount of $MnCl_2{\cdot}4H_2O$ and oxalic acid were each dissolved in 50 mL of distilled water. Under magnetic stirring, the prepared oxalic acid

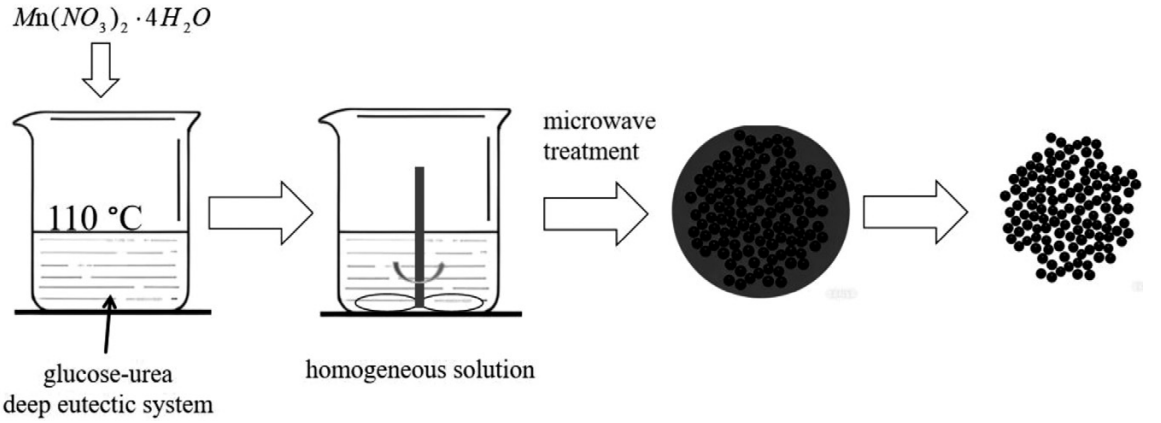

Figure 1: Process-flow diagram of nano MnO_2 prepared by glucose-urea method

solution was dropwise added to the manganese chloride solution. The reaction proceeded for 30 minutes, after which the product was collected by centrifugation and filtration, dried in an oven at 160 °C for 15 h, and then calcined in a muffle furnace at 450 °C for 2 h with a heating rate of 5 °C/min. This sample was labeled as Mn-6.

2.2 Material Characterization

X-ray diffraction (XRD) patterns of the samples were obtained using a SHIMADZU XRD-6100 diffractometer with Cu-Kα radiation (40 kV, 30 mA). The scanning rate was 8°/min over a 2θ range of 10° to 80°. Nitrogen adsorption-desorption measurements were conducted on a Micromeritics ASAP-2460 system. Prior to analysis, the samples were pretreated at 150 °C for 5 h. The specific surface area was calculated using the Brunauer–Emmett–Teller (BET) method, and the pore size distribution was determined by the Barrett–Joyner–Halenda (BJH) method from the adsorption branch. Scanning electron microscopy (SEM) images were acquired using a TESCAN MIRA3 microscope. Before imaging, the samples were dispersed on conductive tape and coated with a thin layer of gold. Raman spectra were recorded on a Thermo Fisher Scientific spectrometer with a 541.5 nm excitation laser, covering a wavenumber range of 100–800 cm^{-1}. Transmission electron microscopy (TEM) was performed on a JEOL JEM-2010 microscope operating at 200 kV. For TEM analysis, the samples were dispersed in absolute ethanol, ultrasonicated for 10 min, and a drop of the suspension was placed on a copper grid and dried under an infrared lamp.

2.3 Catalyst Evaluation

Phenol was used as a model pollutant for evaluating the catalytic performance in phenolic wastewater treatment. The catalytic wet-air oxidation of phenol was carried out in a batch reactor. The setup consisted of a stainless-steel high-pressure autoclave with a 50-mL polytetrafluoroethylene liner. In a typical experiment, 25 mL 2.0 g/L of phenol solution and 0.10 g of catalyst were placed in the PTFE liner and ultrasonicated for 5 minutes. The liner was then sealed in the autoclave. Oxygen was purged into the system three times to ensure an initial oxygen pressure of 0.7 MPa, after which all valves were closed. The autoclave was immersed in an oil bath at 90 °C and reacted for 3 h with stirring at 500 min^{-1}. After cooling, the solution was sampled for analysis. The phenol concentration was determined using the 4-aminoantipyrine spectrophotometric method.[10] The conversion rate was calculated using the following formula:

$$\text{Conversion } (\%) = (C_0 - C) / C_0 \times 100\%,$$

where C_0 is the initial concentration of phenol and C is the concentration after reaction.

The quantitative calibration curve of absorbance versus phenol concentration is shown in **Figure 2**.

3 RESULTS AND DISCUSSION

3.1 Characterization Results

Figure 3 shows the XRD patterns of the prepared manganese oxide samples. As can be seen from the figure, all the samples exhibit distinct diffraction peaks at positions such as 2θ = 23.1°, 32.9°, 38.2°, 45.1°, 49.3°, 55.1°, and 67.4°, corresponding to the characteristic peaks of the (211), (222), (400), (332), (431), (440), and (631) crystal planes of α-Mn_2O_3 (PDF#41-1442). This confirms that the synthesized product is α-Mn_2O_3. The Mn-1 to Mn-5 series of samples were prepared to investigate the effect of varying amounts of urea while keeping the ratio of glucose to manganese nitrate constant. As the amount of urea increases, the peak intensity first weakens and then strengthens. Mn-3 exhibits the weakest characteristic peak intensity, indicating the lowest crystallinity and smallest particle size at this point. This suggests that the addition of urea can effectively regulate

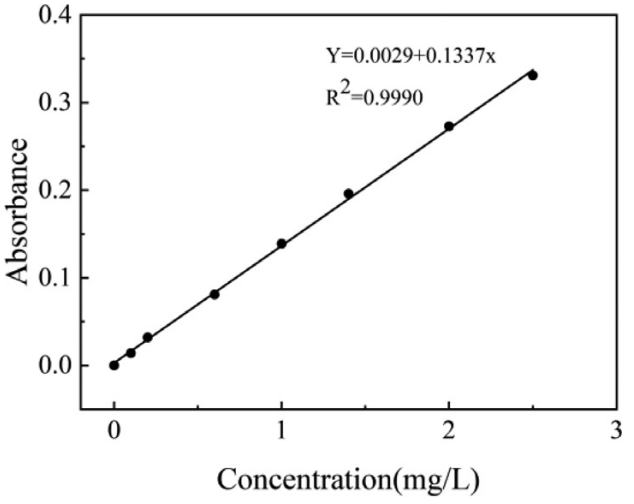

Figure 2: Standard curve of phenol solution

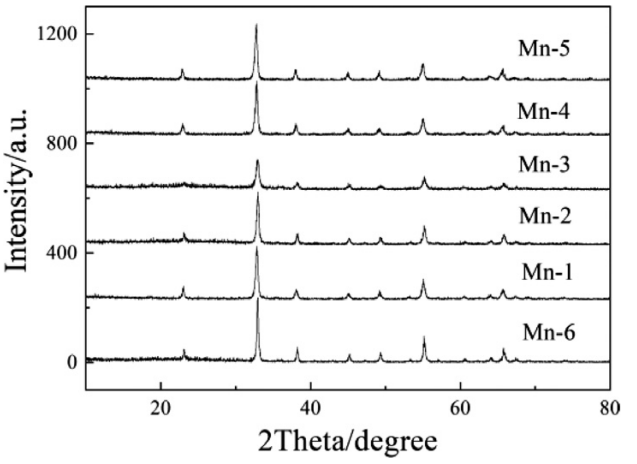

Figure 3: XRD patterns of the prepared manganese oxide samples

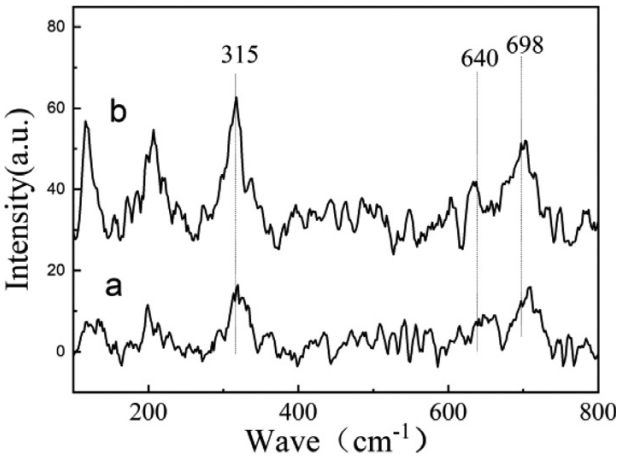

Figure 4: Raman spectra of Mn-3 and Mn-6 (a: Mn-3; b: Mn-6)

the crystallinity of manganese oxide. The manganese oxide prepared by the precipitation method shows the strongest characteristic peaks, indicating the largest particle size. The particle sizes of catalysts Mn-1, Mn-2, Mn-3, Mn-4, Mn-5, and Mn-6 were calculated using the Scherrer formula (results shown in Table 1), and are 26.3 nm, 25.6 nm, 21.2 nm, 25.1 nm, 25.7 nm, and 31.0 nm, respectively.

Mn-3 (template method) and Mn-6 (precipitation method) were selected as representative samples for comparison. **Figure 4** shows the Raman spectra of Mn-3 and Mn-6 as representative manganese oxides. Generally, the characteristic peaks of α-Mn_2O_3 in ex-situ Raman spectra appear at Raman shifts of 307 cm^{-1}, 637 cm^{-1}, and 686 cm^{-1}.[11] Both Mn-3 and Mn-6 exhibit similar characteristic peaks near these three positions, indicating that they have similar crystal structures. The peak near 315 cm^{-1} is attributed to the out-of-plane bending of α-Mn_2O_3, the peak near 640 cm^{-1} is attributed to the asymmetric stretching vibration of bridged oxygen species (Mn-O-Mn), and the peak near 698 cm^{-1} is attributed to the symmetric stretching vibration mode of the α-Mn_2O_3 group.[12] The Raman characterization results further confirm that the synthesized material is α-Mn_2O_3. Additionally, comparing the two samples, it can be observed that the Raman characteristic peaks of Mn-3 at 315 cm^{-1} and 698 cm^{-1} are relatively broad and weak, indicating lower crystallinity, i.e., Mn-3 has a smaller particle size distribution, which is consistent with the XRD analysis results.

The pore structures of the prepared manganese oxide samples were analyzed using nitrogen adsorption-desorption characterization (**Figure 5**). All samples conform to the characteristics of typical Type-II isotherms and exhibit H3-type hysteresis loops in the high-pressure region, indicating that the samples have accumulated pores formed by particle stacking, and the pores have mesoporous characteristics. Analysis using the BJH model shows that most pore sizes are concentrated in the range 14–33 nm, falling within the mesoporous size range. The specific surface areas of the samples were calculated using the BET model. The specific surface areas of samples Mn-1, Mn-2, Mn-3, Mn-4, Mn-5, and Mn-6 are 16.1 m^2/g, 21.8 m^2/g, 39.7 m^2/g, 32.4 m^2/g, 23.3 m^2/g, and 9.6 m^2/g, respectively (**Table 1**).

Table 1: Physicochemical properties of the prepared manganese oxide samples

Samples	Specific surface areas (m^2/g)	Total volume (cm^3/g)	Average pore size (nm)	Crystal size[a] (nm)
Mn-1	16.1	0.188	32.7	26.3
Mn-2	21.8	0.131	29.2	25.6
Mn-3	39.7	0.222	24.2	21.2
Mn-4	32.4	0.185	25.6	25.1
Mn-5	23.3	0.189	32.1	25.7
Mn-6	9.6	0.028	13.6	31.0

[a]Calculated from XRD data using the Scherrer formula.

Mn-3 exhibits the highest specific surface area among all samples, while Mn-6, prepared by the precipi-

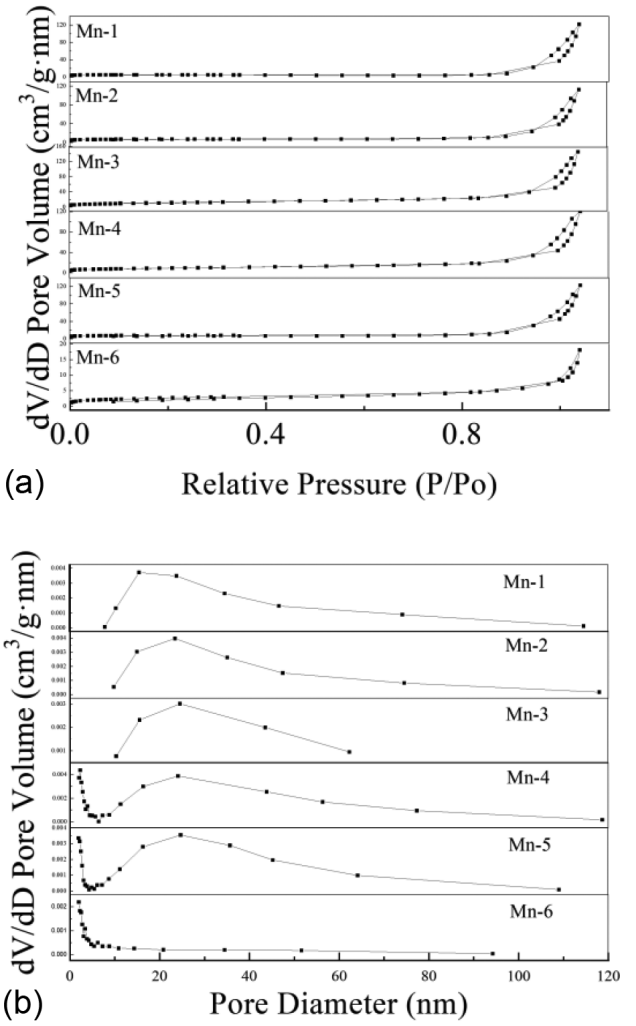

Figure 5: Nitrogen adsorption-desorption analysis of manganese oxide samples

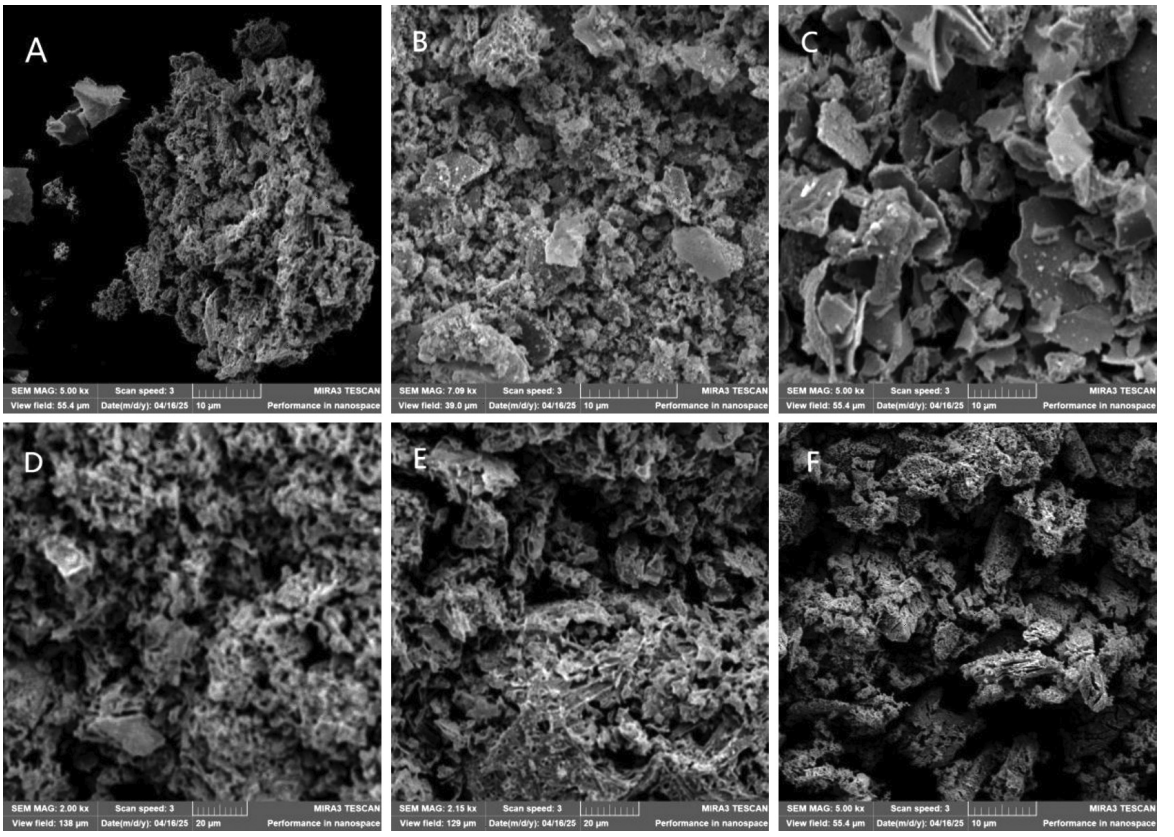

Figure 6: SEM images of Mn_2O_3 samples (A: Mn-1; B: Mn-2; C: Mn-3; D: Mn-4; E: Mn-5; F: Mn-6)

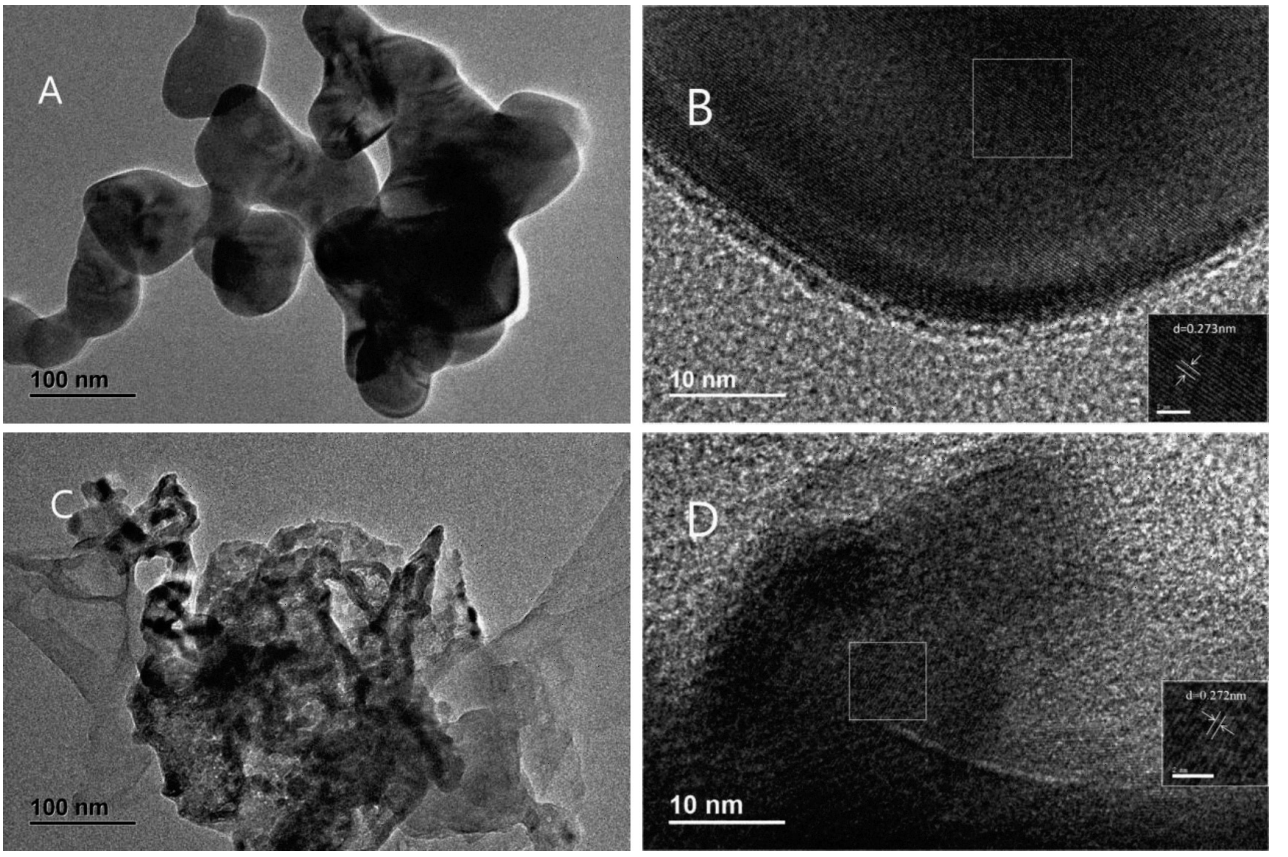

Figure 7: TEM images of Mn_2O_3 samples (A: Mn-6; C: Mn-3) and HRTEM images (B: Mn-6; D: Mn-3)

tation method, has the smallest specific surface area. Additionally, its pore size is 14 nm, smaller than that of all samples prepared by the glucose-urea method. Generally, larger specific surface areas and pore structures are favorable for the adsorption and diffusion of products, potentially offering advantages in adsorption and catalytic reactions. This indicates that the samples prepared by the glucose-urea method have certain advantages.

Figure 6 shows the SEM images of the prepared manganese oxide samples. As can be seen from the images, Mn-1, Mn-2, and Mn-3 exhibit a mixed accumulation of irregular particles and sheet-like structures, while Mn-4, Mn-5, and Mn-6 show structures composed of irregular particle accumulations. Among them, Mn-3 has a more pronounced sheet-like accumulation structure, which may be the main reason for its larger specific surface area. Mn-6 forms a relatively dense structure with significant aggregation, which may be the main reason for its smaller specific surface area.

Figure 7 shows the TEM images of the Mn_2O_3 samples. It can be observed that Mn-6 exhibits a spherical morphology with a larger particle size of approximately 70 nm. Mn-3, on the other hand, shows relatively well-dispersed spherical particles of about 12–15 nm. It is worth noting that although Mn-6 and Mn-3 have different particle sizes, their lattice-fringe spacings are 0.273 nm and 0.272 nm, respectively, both corresponding to the (222) crystal plane of α-Mn_2O_3. This confirms that both have the α-Mn_2O_3 crystal structure, which is consistent with the XRD analysis.

Glucose and urea both play important roles in material preparation. Through various mechanisms such as carbonization, pore formation, exothermic or endothermic reactions, they influence the structure and properties of the final material. In the literature, it is generally believed that glucose carbonizes at high temperatures and acts as a hard template, reducing the particle aggregation.[11,13,14] Urea, on the other hand, has two main effects in the conversion of nitrates: one is its decomposition to produce gases, which create pores in the formed material and carry away a significant amount of heat, reducing particle aggregation;[11,13] the other is that the reaction between urea and nitrates generates heat, which exacerbates the aggregation of oxides[14]. These two effects coexist in the material-preparation process, and it is necessary to balance them and control the reaction conditions to achieve the desired material structure and properties.

The above characterization shows that as the amount of urea added gradually increases from 2.5 g to 20 g, the particle sizes of the prepared Mn-1 to Mn-5 samples first decrease and then increase, reaching the smallest particle size in Mn-3. This indicates that as the urea addition increases from 2.5 g to 10 g (corresponding to samples Mn-1, Mn-2, and Mn-3), urea primarily inhibits crystal aggregation and reduces particle size. However, when the urea addition further increases from 10 g to 20 g (corresponding to samples Mn-3, Mn-4, and Mn-5), urea mainly promotes crystal aggregation, leading to an increase in particle size.

In summary, α-Mn_2O_3 crystals were successfully prepared via microwave-assisted carbonization in a glucose-urea system. The amount of urea added during preparation regulates the crystallinity, grain size, specific surface area, and pore structure of the material. Among the samples, Mn-3 exhibits the lowest crystallinity, smallest grain size, and largest specific surface area. Its unique sheet-like accumulation structure is the main reason for its high specific surface area. In contrast, Mn-6, prepared by the traditional precipitation method, exhibits large grain size, small specific surface area, and a dense structure. The above characterization results provide experimental evidence for understanding the dual competitive mechanisms of pore formation and aggregation promotion by urea during material formation and demonstrate that the physicochemical properties of nano manganese oxide can be regulated by optimizing the amount of urea added.

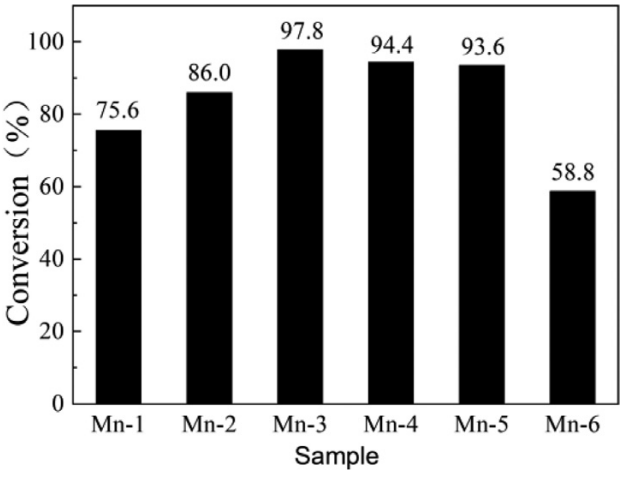

Figure 8: Catalytic performance of nano-Mn_2O_3 samples in wet-oxidation of phenol

3.2 Catalytic Performance Evaluation

Figure 8 shows the catalytic performance of the prepared manganese oxides in the wet catalytic oxidation of phenol. Under conditions of 90 °C and an oxygen pressure of 0.7 MPa, Mn-3 exhibits the highest phenol conversion, reaching 97.8 % after 3 h of reaction. Under the same conditions, the phenol conversions of Mn-1, Mn-2, Mn-4, and Mn-5 are 75.6 %, 86 %, 94.4 %, and 93.6 %, respectively. In contrast, Mn-6, prepared by the precipitation method, shows the lowest phenol conversion of only 58.8%. This indicates that the manganese oxides prepared by the glucose-urea system have advantages.

Research shows that the crystal structure of manganese oxide has an impact on its performance in the wet oxidation of phenol.[15] Different crystal structures can alter the oxygen activation capacity. Among the four crys-

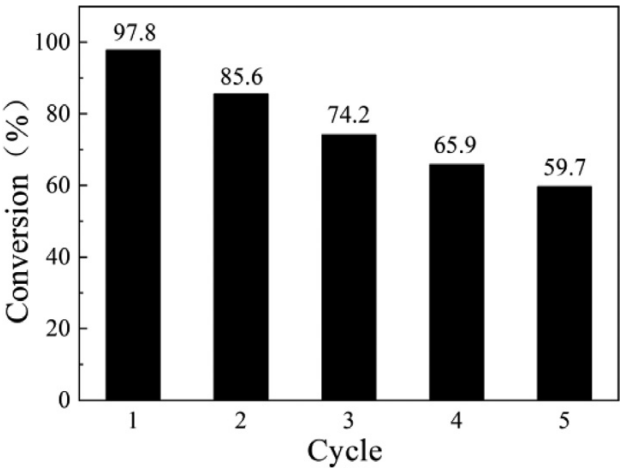

Figure 9: Stability test of Mn-3 in wet oxidation of phenol

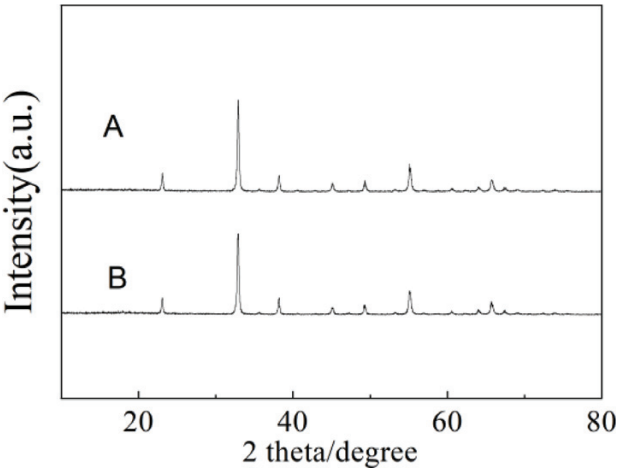

Figure 10: XRD patterns of Mn-3 sample before and after reaction (A: before reaction; B: after 5 reactions)

tal types of manganese oxide studied (α-Mn_2O_3, β-Mn_2O_3, γ-Mn_2O_3, and δ-Mn_2O_3), α-Mn_2O_3 exhibited the best catalytic performance. The XRD characterization of this study shows that both the Mn_2O_3 synthesized by the glucose-urea method and the traditional precipitation method have the same α-crystal structure. Therefore, the influence of crystal structure on catalytic activity differences can be excluded. Further analysis shows that the XRD, TEM, and Raman spectra of Mn-3 indicate lower crystallinity, suggesting the possible presence of richer surface defects (such as oxygen vacancies). These defect sites can effectively promote the oxygen activation process in phenol oxidation reactions. Additionally, lower crystallinity leads to a reduction in the grain size of α-Mn_2O_3, exposing more active sites on the catalyst and enhancing the contact probability between phenol molecules and the catalyst surface. It is worth noting that the optimized urea addition effectively regulates the pore structure of the material, forming larger mesopores, which facilitates the diffusion of phenol and oxygen and the desorption of products, thereby reducing the mass-transfer resistance. In summary, the high catalytic activity of Mn-3 is mainly attributed to three key factors: (1) abundant surface defects promoting oxygen activation; (2) a larger specific surface area (39.7 m^2/g) providing more active sites; and (3) an optimized mesoporous structure improving mass transfer efficiency.

Stability is one of the key indicators for evaluating catalyst performance. The stability test results for Mn-3 are shown in **Figure 9**. After each evaluation, the reacted Mn-3 catalyst was filtered, washed with distilled water, dried at 80 °C, and then used for the next evaluation. As can be seen from the figure, after five reaction cycles, Mn-3 still maintains a conversion rate of about 60 %, indicating good stability. **Figure 10** shows the XRD patterns of Mn-3 before and after the reaction. It can be seen that its characteristic diffraction peaks did not change significantly, indicating that the crystal structure of the catalyst remained stable under the reaction conditions, and the reaction process did not significantly affect its structure.

4 CONCLUSIONS

This study prepared a series of nano α-Mn_2O_3 catalysts via a microwave-assisted method in a glucose-urea system and investigated the effect of urea addition on the material structure and catalytic performance. The results show that the urea content regulates the crystallinity, specific surface area, and pore structure of manganese oxide. Among the samples, the optimized Mn-3 exhibited the best catalytic performance, achieving a phenol conversion of 97.8 % within 3 h under conditions of 90 °C and 0.7 MPa O_2, higher than the 58.8 % conversion of Mn-6 prepared by the traditional precipitation method. Combined with techniques such as XRD, Raman spectroscopy, nitrogen adsorption-desorption, and SEM, it was found that Mn-3 has the smallest grain size, high specific surface area, and abundant mesoporous structure, which collectively contribute to its excellent catalytic activity. Additionally, Mn-3 maintained a phenol conversion of 60 % after 5 cycles, demonstrating good stability.

Acknowledgment

The authors acknowledge the support from the 2022 Xingtai Young Scientific and Technological Talent Project: Application of Nanocatalytic Technology in Green Conversion of Coal-Based Products (2022zz103).

5 REFERENCES

[1] Liotta, L. F.; Gruttadauria, M.; Carlo, G. D.; Perrini, G.; Librando, V., Heterogeneous catalytic degradation of phenolic substrates: Catalysts activity. Journal of Hazardous Materials, 162 (**2009**), 588–606, doi:10.1016/j.jhazmat.2008.05.115

[2] Ma, P.; Zhang, N.; Shi, J.; Lu, H.; Fan, J.; Li, M.; Deng, Q.; Fang, Z.; Chen, B.; Zheng, Q.; Ye, S., Oxygen activation and transfer for cata-

lytic wet-air oxidation of wastewater: a short review. RSC Advances, 14 (**2024**), 37618–37627. doi:10.1039/D4RA04351K

[3] Li Z.; Yang. Y.; Axel R.et al.,Tuning morphology, composition and oxygen reduction reaction (ORR) catalytic performance of manganese oxide particles fabricated by γ-radiation induced synthesis, Journal of Colloid and Interface Science, 583 (**2021**), 71–80. doi:10.1016/j.jcis.2020.09.011

[4] Gu, H.; Yokoya, T.; Kang, L.et al., Oxygen vacancy formation as the rate-determining step in the Mars-van Krevelen mechanism, American Chemical Society, 2024. doi:10.26434/chemrxiv-2024-nbzhr

[5] Shi, J.; Qi, T.; Sun, B. C., Catalytic oxidation of benzyl alcohol over MnO_2: Structure-activity description and reaction mechanism. Chemical engineering journal 440 (**2022**), 135802,1–11. doi:10.1016/j.cej.2022.135802

[6] Yang, Y.; Zhang, P.; Hu, K.; Zhou, P.; Wang, Y.; Asif, A. H.; Duan, X.; Sun, H.; Wang, S. Crystallinity and valence states of manganese oxides in Fenton-like polymerization of phenolic pollutants for carbon recycling against degradation, Applied Catalysis B: Environmental, 315 (**2022**), 121593–121605. doi:10.1016/j.apcatb.2022.121593

[7] Zhang, J.; Zhuang, T.; Liu, S.; Zhang, G. C.; Huo, K. Catalytic ozonation of phenol enhanced by mesoporous MnO_2 prepared through nanocasting method with SBA-15 as template, Journal of Environmental Chemical Engineering, (8)2020, 103967-103976, doi:10.1016/j.jece.2020.103967

[8] Tejashwini, D. M.; Harini, H. V.; Nagaswarupa, H. P.; Naik, R.; Deshmukh, V. V.; Basavaraju, N., An in-depth exploration of eco-friendly synthesis methods for metal oxide nanoparticles and their role in photocatalysis for industrial dye degradation. Chemical Physics Impact 7 (**2023**), 100355, 1–29. doi:10.1016/j.chphi.2023.100355

[9] Yi S., Chen Z., Lai P., Jiang. X., Effect of NaCl on Nano CeO_2 Particles Prepared by Glucose-Urea Method. Journal of Wuhan Institute of Technology 45 (2023), 390–394. doi:10.19843/j.cnki.CN42-1779/TQ.202301011

[10] Portela Miguélez, J. R.; López Bemal, J.; Nebot Sanz, E.; Martínez de la Ossa, E., Kinetics of wet air oxidation of phenol. Chemical Engineering Journal, 67 (**1997**), 115–121. doi:10.1016/S1385-8947(97)00025-9

[11] Li, J.; Xie, X.; Zhong, W.; Liu, Z.; Jiang, W.; Hu, G., Preparation of inexpensive S-doped porous carbons for high-performance supercapacitors. Diamond and Related Materials, 142 (2024), 110856, 1–10. doi:10.1016/j.diamond.2024.110856

[12] Han Y., Chen, L., Ramesh, K., Widjaja, E., Chilukoti, S., Surjami, I. K., Chen, J., Kinetic and spectroscopic study of methane combustion over α-Mn_2O_3 nanocrystal catalysts. Journal of Catalysis, 253 (**2008**), 261–268. doi:10.1016/j.jcat.2007.11.010

[13] Wang, R.; Zhao, Y.; Xu, C.; Liu, Y.; Wu, W.; Zhao, D., Enhanced removal of Pb^{2+}, Cd^{2+} and Zn^{2+} ions on porous carbon from aqueous solutions by capacitive deionization: Performance study and underlying mechanism. Surfaces and Interfaces, 45 (**2024**), 103858–103870. doi:10.1016/j.surfin.2024.103858

[14] Gachlou, Z., Razavi, A., Torabi, N., Magnetically separable Cu-Fe nanophotocatalyst with enhanced photocatalytic performance under visible-light irradiation: Optimizing the fuel type and heating approach in the synthesis process. Inorganic Chemistry Communications 161 (**2024**), 112042, 1–14. doi:10.1016/j.inoche.2024.112042

[15] Wu, Q.; Ma, L.; Gong, W.; Li, X.; Zhao, S.; Khan, A.; Li, W.; Xu, A., Phase-dependent reactivity of MnO_2 catalysts for permanganate activation: Insight into the role of surface-adsorbed MnO_4^- species. Journal of Cleaner Production, 419 (**2023**), 138325-138337. doi:10.1016/j.jclepro.2023.138325